Relationship Between Microbial Growth and Hydraulic Properties at the Sub-Pore Scale

Neda Hassannayebi[1] · Boris Jammernegg[1] · Johanna Schritter[2] · Pit Arnold[1] ·
Frieder Enzmann[3] · Michael Kersten[3] · Andreas P. Loibner[2] · Martin Fernø[4] ·
Holger Ott[1]

Abstract

Accumulation of microbial biomass and its influence on porous media flow were investigated under saturated flow conditions. Microfluidic experiments were performed with model organisms, and their accumulation was observed in the pore space and on the sub-pore scale. Time-lapse optical imaging revealed different modes of biomass accumulation through primary colonization, secondary growth, and filtration events, showing the formation of preferential flow pathways in the flooding domain as result of the increasing interstitial velocity. Navier–Stokes–Brinkmann flow simulations were performed on the segmented images—a digital-twin approach—considering locally accumulated biomass as impermeable or permeable based on optical biomass density. By comparing simulation results and the experimental responses, it was shown that accumulated biomass can be considered as a permeable medium. The average intra-biomass permeability was determined to be 500 ± 200 mD, which is more than a factor of 10 larger than previously assumed in modeling studies. These findings have substantial consequences: (1) a remaining interstitial permeability, as a result of the observed channel formation and the intra-biomass permeability, and (2) a potential advective nutrient supply, which can be considered more efficient than a purely diffusive supply. The second point may lead to higher metabolic activity and substrate conversion rates which is of particular interest for geobiotechnological applications.

✉ Holger Ott
holger.ott@unileoben.ac.at

1   Department Petroleum Engineering, Parkstraße 27, 8700 Montanuniversität Leoben, Austria

2   Institute of Environmental Biotechnology, University of Natural Resources and Life Sciences Vienna, 3430 Tulln a.d. Donau, Austria

3   Institute of Geosciences, Johannes-Gutenberg University, 55099 Mainz, Germany

4   Department of Physics and Technology, University of Bergen, 5020 Bergen, Norway

1 Introduction

The presence and metabolic activity of microbial life in the subsurface are likely to influence the hydrodynamic properties of porous aquifers and reservoir rocks. Microbiological processes can be used deliberately in subsurface engineering, e.g., (i) for remediating contaminated soils and groundwater bodies by breaking down toxic chemicals (MacQuarrie et al. 1990), (ii) for geo-methanation processes by in situ conversion of gases like carbon dioxide and hydrogen to methane (Götz et al. 2016; Strobel et al. 2020), and (iii) for microbial enhanced oil recovery (MEOR) through the production of in situ surfactants to reduce the interfacial tension between oil and water, or through the production of bio-polymers to establish flow barriers in exploited zones of oil fields (Surasani et al. 2013; Baveye et al. 1998; Lazar et al. 2007). In all these applications, products of microbial metabolism including bacterial cells themselves modify the hydraulic reservoir properties and the mobility of fluids or substances dissolved therein. Such mechanisms can be deliberately initiated, e.g., by injecting nutrients (in the context of this study, the term 'nutrients' comprises substance needed for microbial growth such as growth substrates, minerals and electron acceptors) to stimulate the proliferation of indigenous microorganisms (bio-stimulation) or by injecting competent exogenous microorganisms along with amendments to trigger desired sub-surface processes (bio-augmentation). However, a lack of understanding of the microbial biomass distribution and the related interactions with porous media may easily result in unwanted effects such as bioclogging (Baveye et al. 1998; Hommel et al. 2018). Excessive enrichment of biomass may lead to a reduction in porosity and permeability, i.e., injectivity of the porous medium.

The prediction of underground flows requires a good knowledge of the hydraulic rock properties; with saturated flow conditions the hydraulic properties are predominantly represented by porosity (ϕ) and permeability (K). In some applications such as MEOR and underground gas storage, two or more fluid phases are present in the pore space, and multiphase flow effects need to be considered. For a complete description of two-phase flow, the capillary pressure ($p_C(S_W)$) and relative phase permeability ($k_r(S_W)$) saturation functions play decisive roles in addition to ϕ and K. If microbial biomass accumulates in the pore space of a formation rock and the porosity decreases, all other parameters change as well. In the simplest case, this change may be described by introducing the relationship between porosity and absolute permeability ($K(\phi)$). Even in multiphase flow cases, a reduction in ϕ is often considered to change only K. Porosity and permeability are generally related by power laws (Hommel et al. 2018); a reduction in K is therefore very sensitive to a reduction in ϕ. This makes the $K(\phi)$ relationship a critical factor in all reactive transport problems, regardless of whether precipitation is inorganic or organic. Whereas inorganic precipitates are often considered solid and rigid, microbial biomass appears porous and contains water and tends to be soft in nature (Hommel et al. 2018). Note that we use the term "biomass" for an accumulation of microbial cells (and metabolic products) with flow between the cells rather than within or through the cells.

The extent to which K depends on a reduction in ϕ and the exact shape of the $K(\phi)$ relationship have been found to depend on the exact distribution of the biomass in the pore space and on the larger scale as outlined below. The intra-biomass hydraulic properties also play a substantial role; the biomass permeability may affect the porous medium's overall hydraulic properties and determines the intra-biomass transport, and hence, the nutrient supply to the microbial cells in the accumulated biomass.

Biofilms arise in natural and engineered systems—preferentially in aqueous environments—via (a) microorganism transport and attachment, (b) biofilm growth, and (c) detachment of clusters and streamers and their propagation (Gerlach and Cunningham 2010). During the growth process, the enclosing cells produce extracellular polymeric substances (EPSs) to increase the cohesive strength of the biofilm. Furthermore, the EPS matrix acts as a nutrient reservoir. The resulting intra-biomass hydraulic properties are largely unknown. In most hydraulic simulation studies, microbial biomass is considered impermeable as outlined further below. This implies that the nutrient transport within the biomass is either not explicitly addressed or occurs only by diffusion; advective nutrient transport is therefore often neglected. However, studies on biofilms have revealed that the morphology of a biofilm is prevalently heterogeneous and may contain channels and voids (i.e., internal porosity) and hence may facilitate advective transport (Flemming et al. 2016). As a result, biofilms contain not only immobile water but also a considerable amount of mobile water; the total percentage of water in biofilms can be as high as 97%.

Under starvation conditions in microfluidics experiments, biomass predominantly accumulated in the pore bodies and later in the pore throats (Kim and Fogler 2000). Pore network modeling was used to simulate biomass evolution in the pore space and the associated pressure response. The biofilm growth rate was found to be directly linked to the available nutrient concentration, but nutrient transport inside the biofilms was not explicitly modeled. In a study by Thullner et al. (2002), microbial growth was assumed to occur in colonies and biofilms, and conductivity was computed for both scenarios by pore network modeling. It was found that the growth in colonies leads to a much stronger dependency of K on a reduction in ϕ. Biomass growth in colonies was not linked to the nutrient concentration in the pores, but to the pore size; smaller pore sizes were first filled completely, followed by the next class of pore sizes, successively removing the smallest pores from the network. For film growth, nutrient availability near the biofilm site was considered (growth-limiting solute nutrient), accounting for microbial growth, decay and detachment by shear forces. However, intra-biomass transport was not explicitly considered.

Thullner and Baveye (2008) introduced permeable biomass in pore network modeling; earlier models demonstrated impermeable biomass with only diffusive nutrient transport. A milder overall permeability reduction was found as in column experiments by considering the biomass as microporous and permeable. The intra-biomass flow was not explicitly simulated, but the water in the biomass was set to a higher viscosity. For the permeable case, the viscosity was set to the base viscosity $\times 1000$ (i.e., water in biomass is 1000 times less mobile compared with water in the open pore space). Furthermore, biofilm permeability was found to primarily affect biomass growth and, to a lesser extent, overall hydraulic conductivity; growth tended to be faster with permeable biomass.

Qin and Hassanizadeh (2015) also performed pore network modeling beyond the typical biomass growth assumptions with constant mass exchange coefficients or the mass equilibrium assumption. They explicitly modeled solute transport and exchange with biomass associated with biomass growth. A rate-limiting solute was considered. Similar to the above study, flow in the micropores was also introduced via an increase in viscosity by a factor of 1000 (Thullner and Baveye 2008). Deng et al. (2013) performed direct flow simulations using the Navier–Stokes Brinkman approach, based on column glass-bead reactor experiments reported earlier (Kirk et al. 2012). The simulations, performed in 2D using 2D confocal microscopic images, showed that biomass permeability had a significant impact on the shear stress distribution, and therefore potentially affected biofilm erosion and detachment. The sensitivity of flow fields to biomass permeability directly affected the spatial distribution of where transport is dominated by advection or diffusion.

In the present study, we investigate bacterial growth and transport in a saturated porous medium in microfluidic chips. We combine the experimentally observed biomass distribution and the measured differential pressure with direct numerical simulations based on a "digital twin" approach that directly accounts for the experimentally observed biomass distribution; we determine the $K(\phi)$ relationship by solving the Navier–Stokes–Brinkman equations directly using the binarized experimental images. Similar to previous studies, we consider the accumulated biomass to be microporous and systematically investigate the effective biomass permeability and evaluate the simulated scenarios based on the experimentally observed pressure response; the following cases were considered: (1) the biomass is impermeable, (2) individual permeability values were assigned to the biomass, and (3) a porosity/permeability distribution was assigned based on the grayscale of the recorded images.

With the here applied combined experimental/numerical workflow, we experimentally determine/estimate the intra-biomass permeability. Biomass permeability impacts the overall hydraulic properties ($K(\phi)$) and the nutrient supply, respectively, the biomass growth and chemical conversion rates. This is an important qualitative step beyond the above cited numerical work, which so far assumed biomass distributions and biomass permeability. The work also goes beyond previous experimental work, which imaged the biomass distribution but did not determine the hydraulic system properties.

2 Material and Methods

2.1 Instrumental

To examine the effect of bacterial growth in porous media, time-lapse optical visualization experiments were carried out using etched glass microfluidic chips (micronit.com) fabricated from borosilicate glass. The porous medium is shown in Fig. 1 and is characterized by a uniform etching depth (nominal 20 µm) and a laterally defined heterogeneous 2D pore network (2 cm × 1 cm), with a bifurcating inlet and outlet channel pattern for fluid distribution and collection. The porosity, permeability, and total pore volume were 0.57, 2.5 D, and 2.3 µL, respectively. The lateral average pore size (diameter) was determined to be 280
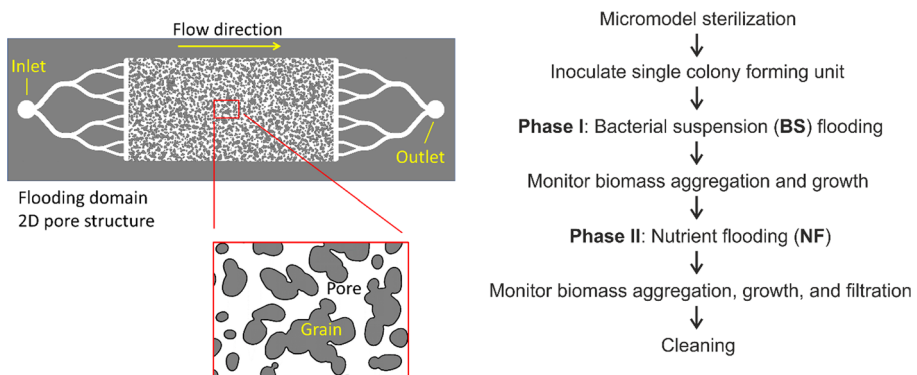

Fig. 1 Left: pore structure (white) of the 2D porous medium with the microfluidic chip's inlet- and outlet-channel patterns. Right: sequential experimental workflow

μm with a distribution width (full width at half maximum—FWHM) of 200 μm. Fluids were injected using a syringe pump (Chemyx Fusion 200), at a constant volumetric flow rate of 0.2 mL/h against ambient pressure. A differential pressure transducer recorded the pressure drop across the micromodel. A Leica DMi8 microscope was used in the majority of experiments to capture high-quality optical images of the porous domain and the fluids and biomass therein. The images of the total porous domain were acquired by an integrated wide-range automated XY table in combination with a stitching software. The images were recorded with a Leica DMC2900 camera with an exposure time of 1 ms and an image pixel size of 1.8 μm. The overall time resolution for imaging the total porous domain was limited by the XY scanning to 35 s. Images of regions of interest (ROI) were partly taken with a Motic AE2000 microscope. The setup was placed in an incubator to keep all elements at a constant temperature of 37 ± 1 °C during the experiments.

2.2 Microorganisms

Lactobacillus casei was used as a model microorganism in microfluidic experiments. This species was selected for several reasons. This non-motile rod-shaped Gram-positive bacterium is small in size and able to grow in oxygen-free environments. It tolerates a wide range of temperature and pH conditions with the optimum being between 30 and 40 °C and 5.5 to 6.2, respectively (Ludwig et al. 2009), conditions that can be found frequently in biogenic reservoirs. Moreover, *L. casei* is a non-pathogen that is easy to cultivate and undemanding in handling. Freeze-dried *L. casei* from a master cell bank established at IFA-Tulln/Boku was suspended in MRS medium (26.1 g MRS broth in 500 mL of aqua dest and autoclaved for 15 min at 121 °C). This culture was streaked on agar (34.1 g MRS agar in 500 mL of aqua dest, autoclaved for 15 min at 121 °C), and incubated overnight at 37 °C. A single colony from the agar plate was used to inoculate the MRS medium which was then incubated at 37 °C.

Optical density of the bacterial suspension at a wavelength of 600 nm (OD_{600}) was used to monitor the progress of cell density over time. The resulting growth curve revealed the stationary phase starting 22 h after inoculation. From the $OD_{600} \approx 2$, we estimate the concentration of the suspension to 10^8 cells/mL. In the following, *L. casei* cultures right from the beginning of the stationary phase diluted by a factor of 5 were used for suspension flooding experiments.

2.3 Flow Experiments

The flow experiments were performed in initially cleaned water-saturated micromodels in two experimental stages. Firstly, a bacterial suspension in the stationary growth phase was flooded through the microfluidic chip to induce initial occupation of the pore space by microbes. Secondly, after ~ 27 h of suspension flooding, a nutrient solution (MRS nutrient broth) was injected; the supply of nutrients triggered exponential growth of dormant bacteria residing in the chip. The deposition, colonization, and transport of microbial cells and aggregates were visualized by optical microscopy during the two subsequent bacterial suspension (BS) and nutrient flooding (NF) steps. The experimental workflow is summarized in Fig. 1. Altogether, 5 replicate experiments were carried out, and the total porous domain (TD) and/or region of interest (ROI) was visualized.

2.4 Image Segmentation and Numerical Modeling

Direct flow simulations were used to characterize the change in hydraulic properties from biomass accumulation, considering the experimentally observed biomass distribution. The simulations were performed on 3D digital twins. For this, we segmented the 2D microscopic images based on their grayscale. In the third dimension, we considered the true vertical profile of the micromodel corresponding to the effective etching depth to match the permeability from a multirate water permeability measurement. The biomass was assumed to homogenously stretch vertically through the micromodel's full depth with only lateral variation in biomass properties. This assumption may underestimate the impact of biomass accumulation in the early experimental phase, but was confirmed during nutrient flooding by confocal microscopy. For the base case, we segmented the images by thresholding into three principal phases using the ImageJ/Fiji software: the solid phase (grains), the aqueous phase, and the biomass. The threshold was set by the visual impression on the optical contrast—lighter gray values were considered being "contaminations" not influencing the fluid flow. It turned out that this assumption underestimated the influence of the biomass on system conductivity. In a second attempt, the lightest gray values were considered as well using the ilastik software, an interactive machine learning and segmentation toolkit (Berg et al. 2019). We utilized the pixel classification module, which assigns labels to pixels based on pixel features (in our case, the grayscale) as well as user annotations. The biomass was segmented into 4 grayscale classes. Several cases were simulated by considering the biomass as (a) impermeable, (b) permeable with single-average permeability values, and (c) permeable with different permeability values according to the segmented gray scale classes. We computed the changes in the flow field and the permeability as a function of biomass accumulation by solving the Navier–Stokes–Brinkman equation directly on the voxel-based images—the digital twin. For the open pore space, the Navier–Stokes equations were solved, while effective permeability values were assigned to the biomass, and the flow was solved using the Brinkman equation to satisfy continuity at the pore/biomass interface. Because the biomass porosity was not included as porosity in the calculated $K(\phi)$ relationship, this approach is not sensitive to the assigned intra-biomass porosity but rather to the intra-biomass permeability, K_{bm}, and its distribution.

The simulations were performed using the GeoDict software package (math2market.com) with its FlowDict module, employing the LIR solver that was developed to solve creeping flow at low Reynolds numbers (Linden et al. 2015). We assumed saturated and incompressible flow of water with a constant viscosity of 0.82 mPa • s, which corresponds to the measured values of the bacterial suspension and the nutrient solution at experimental temperature. This allowed for a proper comparison of the simulation results with the experimentally measured differential pressure. To check the consistency of the model, we assigned a maximum permeability to the biomass, corresponding to the permeability of a plane-parallel gap, which is $W^2/12 = 33$ D (Homsy 1987), where W is the effective etching depth of the micro model. By assigning this value to the areas occupied by biomass, a nearly independent permeability value was found that corresponds to 33 D, the measured permeability of the empty micromodel, which verifies the approach.

Total flooding domain (TD) simulations used no-flow and no-slip conditions on system boundaries perpendicular to the flow direction. In the flow direction, we explicitly modeled the bifurcating inlet and outlet structure of the micromodel and assigned

constant pressure boundary conditions according to the experimentally measured differential pressure. For the ROI model, we used symmetric boundary conditions in the lateral directions, which mirrored the flooding domain at the boundary, allowing for modeling a subdomain without artificial truncation of flow at the ROI boundaries. ROI simulations were performed using a constant differential pressure ($\Delta P = 2000$ Pa) across the domain size in the flow direction, since the experimental differential pressure does not apply to the reduced local domain. This has no consequences, as unlike the TD simulations, the ROI data are not compared to experimental responses.

3 Results

3.1 Biomass Accumulation and Pressure Response

Throughout the flow experiments, biomass distribution and evolution were visualized at different scales. In the first phase, the microbial suspension was transported into the porous domain. Part of the cells attached to solid surfaces and deposited as aggregates in the pore space. We observed deposition in the total domain, predominantly at the inlet and inhomogenously distributed along the injection channel.

The initial conditioning and spatial distribution of biomass largely determined subsequent biomass distribution. Injection of a nutrient solution in the second experimental phase resulted in growth of inoculated biomass that mainly evolved at these sites where
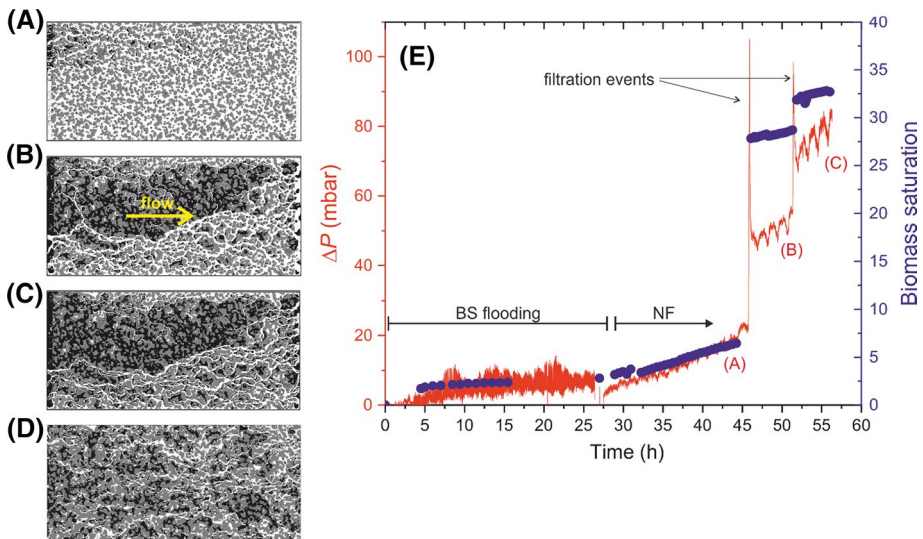

Fig. 2 Images (**a**) to (**c**) show the phase distribution in time steps during a nutrient flooding experiment in the total flooding domain; **a** to **c** after 16, 23, and 29 h of NF, respectively, 43, 50, and 56 h total flooding time. The images are segmented in three phases: white is the open pore space, light gray denotes the grains, and black is the biomass. Images (**c**) and (**d**) show the final states of two different experiments; **d** after 40 h of NF. **e** Correlation of biomass growth and pressure drop across the micromodel. BS and NF refer to the timing of bacterial suspension flooding and nutrient flooding, respectively. The sharp spikes indicate filtration events, as described in the text

cells had originally attached. This spatial–temporal evolution of an extremely heterogeneous case is displayed in images (A) to (C) in Fig. 2. In comparison with image (C), image (D) shows a more homogeneous biomass distribution at a similar stage of a replicate experiment, which depends on the exact biomass distribution during the conditioning. With the growth of biomass, a decreasing amount of pore space is available for the discharge of the injected solution. The flow organized itself in a system of flow channels (preferential pathways) that maintain a certain system hydraulic conductivity.

Increased biomass saturation and clogging of pore space increased the differential pressure (Fig. 2e) and decreased the system permeability. We observed a continuous increase in biomass saturation with higher growth rates in the NF compared to BS flooding, with an accordingly increasing differential pressure. Both data sets provide information on the interplay of porosity–permeability, $K(\phi)$, which is discussed below. The plot shows two events at experimental times of approximately 47 and 52 h. During these events, we observed a highly concentrated microbial suspension flowing through the pore space. The analysis indicated that the suspension originated from releases outside the porous domain. Moreover, although an experimental artifact, we believe that such events are relevant for the field case and simulate local and spontaneous release/detachment of biomass in the borehole or in the porous medium itself. The spike in the differential pressure was not related to the $\sim 20\%$ increase in viscosity compared to the nutrient solution, but was rather an effect of the temporary filtration-related biomass deposition (not captured in the biomass saturation data). After each event, the biomass saturation and the differential pressure continued on a higher level.

In summary, we observed three principal modes of biomass accumulation: (1) initial deposition from suspension, (2) continuous growth by nutrient supply, both of which lead to continuous accumulation of biomass, and (3) filtration events, resulting in a stepwise increase in biomass and differential pressure.

3.2 Biomass Patterns

The microbial biomass organized itself in different structures as exemplified in Fig. 3. Image (A) shows the details of the bacterial suspension in the pore space at rest, with individual cells visible. Under flow conditions, the microbial cells formed aggregates and deposited as biofilms at the grain boundaries (Fig. 3b). Some of the aggregates formed deposits in the middle of the pore space during BS (Fig. 3c) and NF (Fig. 3d) flooding, a typical artifact in microfluidic chips with an upper and lower surface area to which the cells can adhere. The simulated velocity distribution (Fig. 3e) shows that biomass initially accumulated where the flow velocity was relatively low, i.e., in areas with lower shear forces. During NF, these initial seeds grow into patchy structures; this is the onset of a more channelized residual pore space.

Stepwise changes in biomass saturation occurred during filtration of highly concentrated suspensions. Images (f) and (g) in Fig. 3 show an already developed biomass pattern before and after a filtration event. After filtration, elongated structures (streamers) appeared due to accumulation at bifurcating flow channels and valves. It has been reported that the formation of biomass streamers is stabilized in the center of pores at a Reynolds number of Re < 0.01 (Valiei et al. 2012). In the present case, the streamer-like structures develop on the "windward" side of the grain as reported by Secchi et al. (2020) for high flow rates; at the present average flow rate of about 500 μm/s, the microbial velocity is clearly flow dominated. At bacterial velocities dominated by the motility of the swimming bacteria,
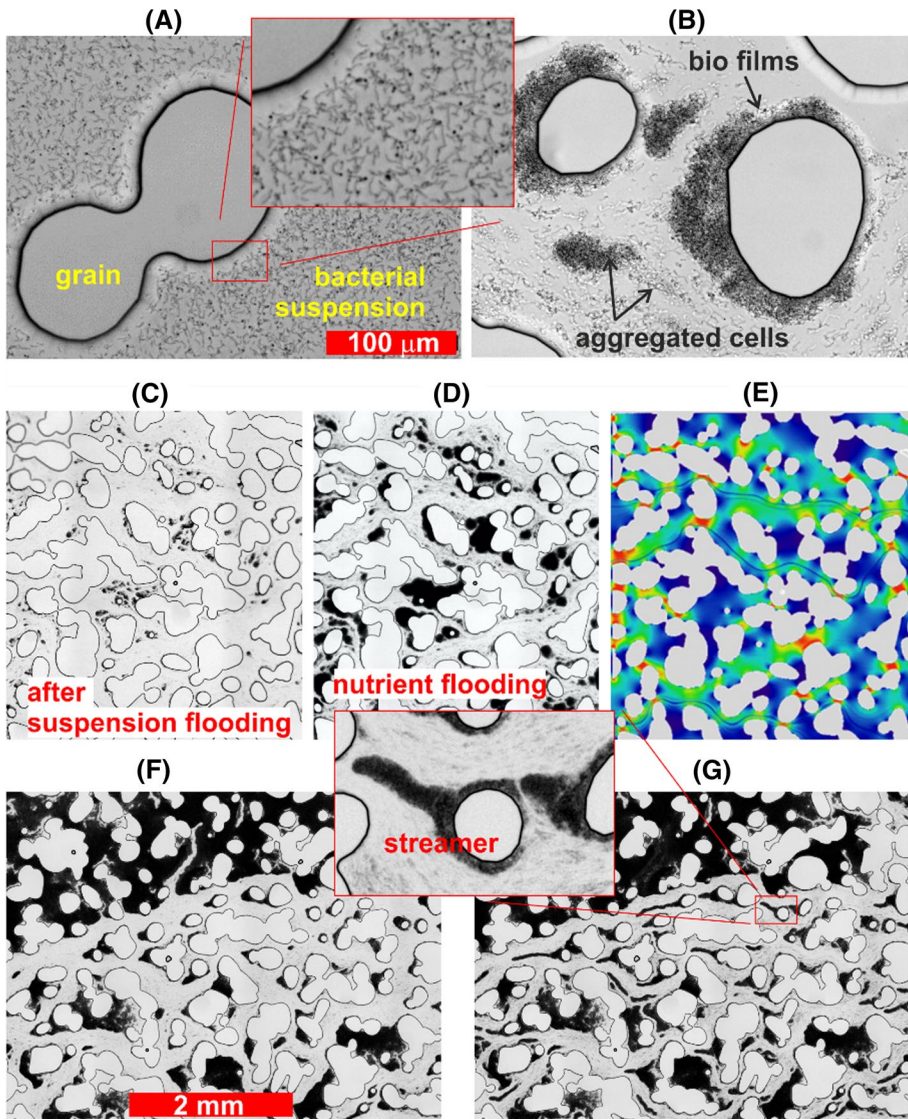
Fig. 3 Microscopic images of bacterial evolution during BS and NF phases. The flow is directed from left to right for all images. **a** Bacterial suspension at rest. **b** Suspended microbial cells adhered to the glass surface to form biofilms. **c** Initially inoculated bacteria after BS flooding and **d** the same volume during NF. **e** Simulated flow velocity field without biomass, for comparison. **f** and **g** Biomass accumulation before and after a filtration event, respectively, and magnification showing the characteristic elongated structure (streamer) that appeared after the filtration event

an accumulation on the leeward side would be expected (Secchi et al. 2020). Such structures support the channelization of the flow. However, the observed shapes may generally be supported by the 2D nature of the porous medium, with its confining upper and lower domain boundaries. In addition to channelization, complete clogging of flow channels was observed during the filtration events. This is best illustrated by the change on a TD-scale

(Fig. 2b to c) showing that the release and subsequent filtration of biomass contributed to the clogging of macroscopic volumes in the flooding domain. However, a remaining open channel system was observed, which is likely due to the increasing shear forces as a result of the decreasing open pore volume at constant volumetric injection rate. Filament-like streamers clogging the pore space by crossing flow channels (Drescher et al. 2013; Rusconi et al. 2011) were not observed.

4 Numerical Interpretation and Discussion

4.1 Numerical Simulation of Hydraulic Properties

Figure 4a shows the simulation results of the total flooding domain at different experimental time steps (base-case simulation). The color code corresponds to the flow velocities, which vary between 0 and 2.4×10^{-3} m/s, as indicated on the scale; with a growth of the biomass and a corresponding reduction in pore space, the flow pathways become narrower, and consequently, the local flow velocity values increased. This development was quantified in the flow-velocity histogram (C) in the same figure, and it clearly tends to show higher peak velocities with biomass accumulation. As a result, the shear rate in the remaining flow channels and the "erosive power" increased. This may be the mechanism that kept these flow channels free of biomass, maintaining a minimum permeability of the
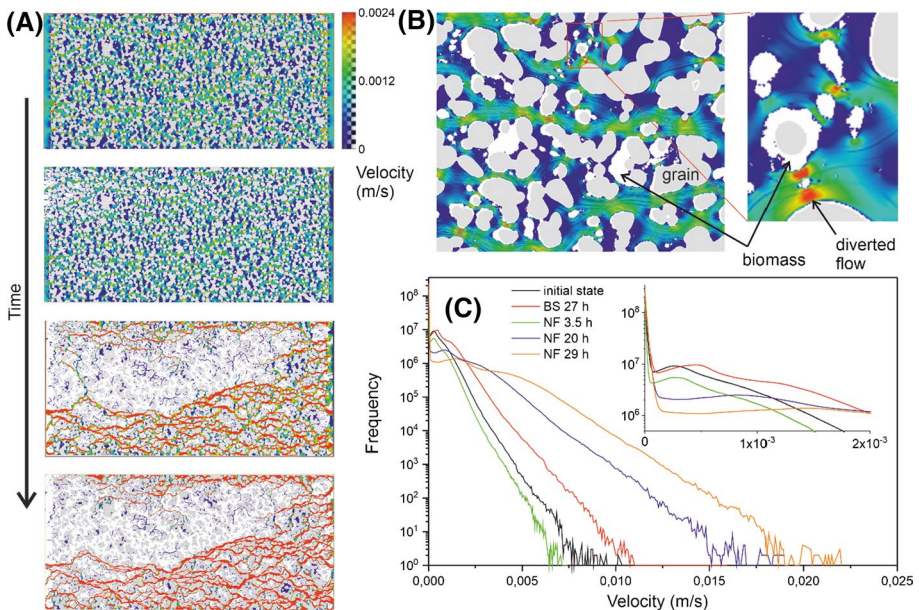

Fig. 4 Results of numerical flow simulations: **a** Simulated velocity field for different biomass accumulations. The time steps correspond to (top down) after BS flooding, during and at the end NF, corresponding to 27, 43, 50, and 56 h of total experimental time. The flow direction is from left to right in all images. The color code is given at the top and is the same for all images. **b** Zoom-in shows the velocity distribution at pore and sub-pore scales. **c** Flow-velocity histogram at different flooding times and the corresponding stages of biomass accumulation
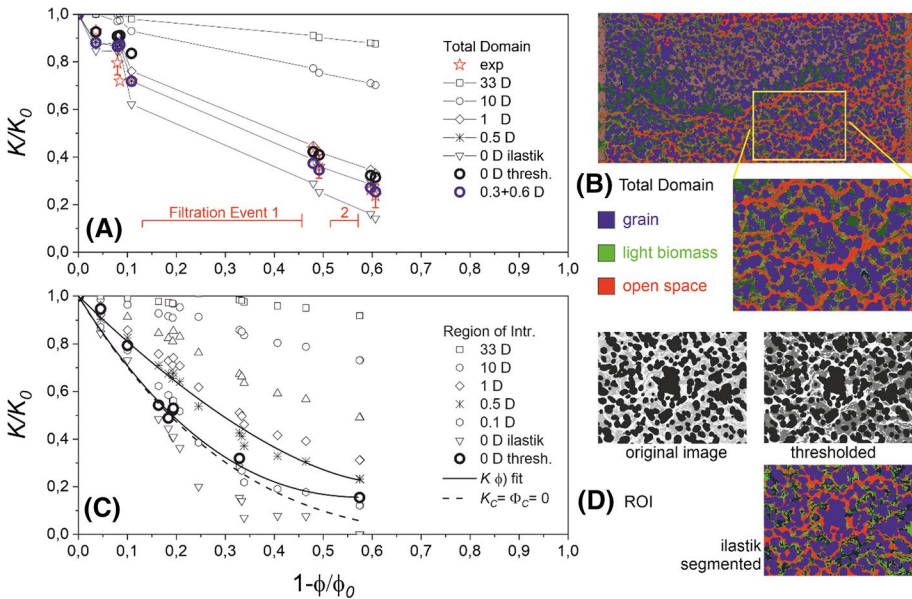
Fig. 5 **a** $K(\phi)$ relationships simulated on the TD for different assumptions with respect to K_{bm}. The simulated data are compared to the experimental response (red stars). **b** ilastik segmented TD (final state). **c** Simulation results from the ROI with power-law fits of selected cases (see text). **d** ROI at late NF stage: original image, base-case (segmented by thresholding in ImageJ/Fiji) and ilastik segmented images. The colors refer to gray-scale levels of the original image

domain, as shown in Fig. 5c (see discussion below). On the other hand, the overall flow field became increasingly heterogeneous and does not represent an REV (representative elementary volume) in a later stage. As shown in Fig. 2c and d, the final states of the different experiments show different degrees of heterogeneity. This may pose a problem for defining the average hydraulic properties in continuum-scale simulations based on pore-scale investigations.

We employed two approaches to investigate the $K(\phi)$ relationship; firstly, we investigated the total domain with the heterogeneously distributed biomass (like in Fig. 2a to c). For this case, both high-resolution images of the total domain and the respective differential pressure data were available. This allows us to compare the experimental determination of the $K(\phi)$ relationship with the simulation results, even with a biomass distribution that does not correspond to an REV. Secondly, we studied a homogeneously occupied ROI (Fig. 5d) in order to study the principal properties of the expected $K(\phi)$ power-law behavior of the system.

4.2 Biomass Permeability K_{bm}

The comparison between simulations and experimental data is given in Fig. 5a and shows that the base-case simulation underestimated the effect of biomass saturation on permeability, with the experimental data showing an even higher impairment that the impermeable-assumed biomass. The deviation was greatest at low biomass saturations, where the gray-scale levels of the biomass are in tendency light. In a further attempt, we considered even slight blurring as

biomass and re-segmented the images assigning different permeability classes on basis of the observed gray scale. The lighter biomass can be calibrated at early experimental time steps and the dark biomass at later time steps during NF. The best match between simulation and experimental data was achieved by assigning $K = 600$ mD to the light fraction (light-green areas in Fig. 5b and $K = 300$ mD to the darker fraction of the biomass. This corresponds to a very low permeability contrast at a high optical contrast in gray scales. Therefore, an average permeability can be given and applied to the system, which is determined to be $K_{bm} = 500 \pm 200$ mD. Impermeable biomass ("solid" in Fig. 5a) did not describe the experimental data. For illustrating the sensitivity, simulation results using average biomass-permeability values in between $K_{bm} = 0$ and $W^2/12$ (the plane-parallel gap) were plotted for comparison. Comparing the obtained K_{bm} to $K_{bm} = W^2/12$ leads to a 50- to 100-times reduction of fluid mobility in the biomass compared to the unoccupied pore space; the biomass is 10 times more permeable than previously considered in simulations (see Introduction).

4.3 The Homogeneous ROI

Figure 5c shows the simulation results for the ROI, for which different permeability values K_{bm} were assigned to the accumulated biomass patches as segmented by ilastik. Using the same approach as for the TD, data were distributed between the two limiting cases, namely impermeable biomass leading to the highest variation of K/K_0, and perfectly permeable biomass assuming "no impairment" due to biomass accumulation. The data are compared to the impermeable base case in the same figure. Accounting for the experimental observation, we described the data using a power-law relationship of the form (Ott et al. 2015):

$$\frac{K - K_C}{K_0 - K_C} = \left(\frac{\Phi - \Phi_C}{1 - \Phi_C} \right)^{\tau},$$

where $\Phi = \phi/\phi_0$, with ϕ being the actual porosity and ϕ_0 the initial porosity of the microfluidic chip, referring to the actual and initial permeability values K and K_0, respectively. K_C is the lowest value to which K can be reduced at a critical reduced porosity Φ_C. This specific form describes the effect of the observed channel formation and the potentially associated finite remaining permeability (Ott et al. 2014). For the impermeable base case (solid), the best fit was achieved using $\Phi_C = 0.4$ (as observed), $K_C/K_0 = 0.23 \pm 0.01$, and $\tau = 2.3 \pm 0.1$, with a reduced χ^2 (deviation) of 10^{-4}. The assumption of vanishing K_C and Φ_C led to $\tau = 3.32 \pm 0.1$ and a reduced χ^2 of 10^{-2} and does not describe the data; both fits are shown in Fig. 5c.

Assigning the earlier derived average biomass permeability of $K_{bm} = 500$ mD leads interestingly to a weaker decay of permeability than for the base case. We fit the data using the same power law as given above. The fit indicates a remaining permeability of $K_C/K_0 = 0.22 \pm 0.06$ (at $\Phi_C = 0.4$), which is now composed of two effects, (1) the formation of preferential pathways and (2) the intra-biomass permeability. K/K_0 decays with an exponent of $\tau = 1.5 \pm 0.3$. It is worth noting that if Φ_C remains a fitting parameter, $\Phi_C \sim 0.4$ turns out to be a robust number.

5 Summary and conclusions

With the here applied combined experimental/numerical workflow, we made a qualitative step and were able to determine/estimate the intra-biomass permeability, which appears to be much larger as previously assumed. The findings have important consequences for the overall hydraulic properties ($K(\phi)$) and the nutrient supply, respectively, bacterial growth and chemical conversion as will be discussed in the following.

The influence of biomass accumulation on the permeability of porous media was investigated using microfluidic under saturated flow conditions. A two-step approach was used to perform replicate experiments: firstly, the microfluidic cell was colonized with microorganisms by bacterial suspension flooding; secondly, a nutrient solution was injected to foster microbial growth. The effects that resulted in the microbial biomass accumulation were primary adsorption, filtration, and bacterial growth. In particular, filtration of upstream released biomass led to a stepwise increase of biomass in the pore space. In contrast, primary and secondary biomass accumulation led to a relatively continuous biomass increase and an associated continuous decrease in permeability.

The spatial distribution of biomass in the pore space results in the formation of preferential flow pathways. Numerical flow simulations have shown that the flow velocity in these remaining pathways increases sharply over time. The associated local increase in kinetic energy may prevent further biomass accumulation, keeping these channels open for flow and preserving a finite permeability, a mechanism that deserves in-depth investigation and final proof.

Biomass accumulation is rather inhomogeneous, and the degree of heterogeneity varies from experiment to experiment; the remaining pore space in the total flooding domain does not necessarily correspond to a representative elementary volume. Numerical simulations were therefore carried out on both a rather homogenously occupied sub-volume of the system and the total domain, which allows to compare the numerical and experimental responses.

Using the segmented images as digital twins, $K(\phi)$ relationships were computed by assigning different constant permeability values and permeability distributions to the biomass. Upon comparing the experimental and numerical results, we conclude that accumulated biomass can be considered as permeable with an average permeability of $K_{bm} = 500$ mD, which is more than 10 times larger than previously assumed in simulations.

These findings have substantial consequences: (1) a remaining interstitial permeability, as a result of the observed channel formation and the in-biomass permeability, and (2) a potential advective nutrient supply, which can be considered as more efficient than purely diffusive supply. Based on the simulated in-biomass flow velocities and observed biomass patch sizes, the Peclet numbers indicate that advection may dominate intra-biomass nutrient transport at 10 mD biomass permeability and above. These findings suggest that microbial biomass in porous media can be efficiently supplied with nutrients so allowing for highly efficient substrate conversion. This is of particular interest for geobiotechnological applications such as subsurface bioremediation or biomethanation processes in natural gas reservoirs.

Declarations

References

Baveye, P., Vandevivere, P., Hoyle, L., B., Deleo, P.C., Sanchez De Lozada, D.: Environmental impact and mechanisms of the biological clogging of saturated soils and aquifer materials. Crit. Rev. Environ. Sci. Technol. **28**, 123–191 (1998). https://doi.org/10.1080/10643389891254197

Berg, S., Kutra, D., Kroeger, T., Straehle, C.N., Kausler, B.X., Haubold, C., Schiegg, M., Ales, J., Beier, T., Rudy, M., Eren, K., Cervantes, J.I., Xu, B., Beuttenmueller, F., Wolny, A., Zhang, C., Koethe, U., Hamprecht, F.A., Kreshuk, A.: ilastik: interactive machine learning for (bio) image analysis. Nat. Methods **16**, 1226–1232 (2019). https://doi.org/10.1038/s41592-019-0582-9

Deng, W., Cardenas, M.B., Kirk, M.F., Altman, S.J., Bennett, P.C.: Effect of permeable biofilm on micro- and macro-scale flow and transport in bioclogged pores. Environ. Sci. Technol. **47**, 11092–11098 (2013). https://doi.org/10.1021/es402596v

Drescher, K., Shen, Y., Bassler, B.L., Stone, H.A.: Biofilm streamers cause catastrophic disruption of flow with consequences for environmental and medical systems. Proc. Natl. Acad. Sci. **110**, 4345 (2013). https://www.pnas.org/content/110/11/4345

Flemming, H.-C., Wingender, J., Szewzyk, U., Steinberg, P., Rice, S.A., Kjelleberg, S.: Biofilms: an emergent form of bacterial life. Nat. Rev. Microbiol. **14**, 563–575 (2016). https://doi.org/10.1038/nrmicro.2016.94

Gerlach, R., Cunningham, A. B.: Influence of biofilms on porous media hydrodynamics. In: Vafai, K. (Ed.). Porous Media: Applications in Biological Systems and Biotechnology, 1st ed., pp. 173–230. CRC Press (2010). https://doi.org/10.1201/9781420065428

Götz, M., Lefebvre, J., Mörs, F., McDaniel Koch, A., Graf, F., Bajohr, S., Reimert, R., Kolb, T.: Renewable power-to-gas: a technological and economic review. Renew. Energy **85**, 1371–1390 (2016). https://doi.org/10.1016/j.renene.2015.07.066

Hommel, J., Coltman, E., Class, H.: Porosity–permeability relations for evolving pore space: a review with a focus on (Bio-)geochemically altered porous media. Transp. Porous Media **124**, 589–629 (2018). https://doi.org/10.1007/s11242-018-1086-2

Homsy, G.M.: Viscous fingering in porous media. Ann. Rev. Fluid Mech. 19, 271–311 (1987). https://doi.org/10.1146/annurev.fl.19.010187.001415

Kim, D.-S., Fogler, H.S.: Biomass evolution in porous media and its effects on permeability under starvation conditions. Biotechnol. Bioeng. **69**, 47–56 (2000). https://doi.org/10.1002/(SICI)1097-0290(20000705)69:1<47::AID-BIT6>3.0.CO;2-N

Kirk, M.F., Santillan, E.F.U., Mcgrath, L.K., Altman, S.J.: Variation in Hydraulic Conductivity with Decreasing pH in a Biologically-Clogged Porous Medium. Intern. J. Greenh. Gas Control **11**, 133–140 (2012). https://doi.org/10.1016/j.ijggc.2012.08.003

Lazar, I., Petrisor, I.G., Yen, T.F.: Microbial enhanced oil recovery (MEOR). Pet. Sci. Technol. **25**, 1353–1366 (2007). https://doi.org/10.1080/10916460701287714

Linden, S., Wiegmann, A., Hagen, H.: The LIR Space Partitioning System Applied to the Stokes Equations. Graph. Models **82**, 58–66 (2015). https://doi.org/10.1016/j.gmod.2015.06.003

Ludwig, W., Schleifer, K.-H., Whitman, W.B.: Order II. Lactobacillales ord. nov. In: Vos, P., Garrity, G., Jones, D., War, N.R., Ludwig, W., Rainey, F.A., Scheifer, K.-H., Whitman, W. (eds.) Bergey's

Manual of Systematic Bacteriology, Volume 3: The Firmicutes. Springer, Dordrecht. ISBN 978-0-387-95041-9 (2009)

Macquarrie, K.T.B., Sudicky, E.A., Frind, E.O.: Simulation of biodegradable organic contaminants in groundwater: 1. Numerical formulation in principal directions. Water Resour. Res. **26**, 207–222 (1990). https://doi.org/10.1029/WR026i002p00207

Ott, H., Andrew, M., Snippe, J., Blunt, M.J.: Microscale solute transport and precipitation in complex rock during drying. Geophys. Res. Lett. **41**, 8369–8376 (2014). https://doi.org/10.1002/2014GL062266

Ott, H., Roels, S.M., De Kloe, K.: Salt precipitation due to supercritical gas injection: I. Capillary-Driven Flow in Unimodal Sandstone. Intern. J. Greenh. Gas Control **43**, 247–255 (2015). https://doi.org/10.1016/j.ijggc.2015.01.005

Qin, C.-Z., Hassanizadeh, S.M.: Pore-network modeling of solute transport and biofilm growth in porous media. Transp. Porous Media **110**, 345–367 (2015). https://doi.org/10.1007/s11242-015-0546-1

Rusconi, R., Lecuyer, S., Autrusson, N., Guglielmini, L., Stone, H.A.: Secondary Flow as a Mechanism for the Formation of Biofilm Streamers. Biophys. J. **100**, 1392–1399 (2011). https://doi.org/10.1016/j.bpj.2011.01.065

Secchi, E., Vitale, A., Miño, G.L., Kanstsler, V., Eberl, L., Rusconi, R., Stocker, R.: The effect of flow on swimming bacteria controls the initial colonization of curved surfaces. Nat. Commun. **11**, 2851 (2020). https://doi.org/10.1038/s41467-020-16620-y

Strobel, G., Hagemann, B., Huppertz, T. M., Ganzer, L.: Underground bio-methanation: Concept and potential. Ren. Sust. En. Rev. **123**, 109747 (2020). https://doi.org/10.1016/j.rser.2020.109747

Surasani, V.K., Li, L., Ajo-Franklin, J.B., Hubbard, C., Hubbard, S.S., Wu, Y.: Bioclogging and permeability alteration by L. mesenteroides in a sandstone reservoir: a reactive transport modeling study. Energy Fuels **27**, 6538–6551 (2013). https://doi.org/10.1021/ef401446f

Thullner, M., Baveye, P.: Computational pore network modeling of the influence of biofilm permeability on bioclogging in porous media. Biotechnol. Bioeng. **99**, 1337–1351 (2008). https://doi.org/10.1002/bit.21708

Thullner, M., Zeyer, J., Kinzelbach, W.: Influence of microbial growth on hydraulic properties of pore networks. Transp. Porous Media **49**, 99–122 (2002). https://doi.org/10.1023/A:1016030112089

Valiei, A., Kumar, A., Mukherjee, P.P., Liu, Y., Thundat, T.: A web of streamers: biofilm formation in a porous microfluidic device. Lab Chip **12**, 5133–5137 (2012). https://doi.org/10.1039/C2LC40815E